Crystal Phase and Composition Synergy for Optimized Optoelectronic Performance and Carrier Dynamics in $Rb_2Au_2X_6$(X=Cl, I) Perovskites

Xifeng Fu[†1,2,3,4], Xue Li[†1,2,3,4], Chang Liu[1,2,3,4], Jin Liu[1,3,4], Sai Guo[1,2,3,4], Zi-Ang Nan[1,3,4], Peng Gao[1,2,3,4], Lingyi Meng*[1,2,3,4]

1. State Key Laboratory of Functional Crystals and Devices, Fujian Institute of Research on the Structure of Matter, Chinese Academy of Sciences, Fuzhou, Fujian 350002, P.R. China.
2. College of Chemistry and Materials Science, Fujian Normal University, Fuzhou 350007, P. R. China
3. Xiamen Key Laboratory of Rare Earth Photoelectric Functional Materials, Xiamen Institute of Rare Earth Materials, Haixi Institutes, Chinese Academy of Sciences, Xiamen 361021, P. R. China
4. Fujian College, University of Chinese Academy of Sciences, Fuzhou, Fujian 350002, P. R. China.

†These authors contributed equally to this work.

*Corresponding authors. E-mail: lymeng@fjirsm.ac.cn (L. Meng)

Experimental characterization method

X-ray diffraction (XRD).

XRD spectra corresponding to the film samples were collected via a Rigaku Miniflex 600 X-ray diffraction system (Japan) operated with Cu Kα irradiation.

X-ray crystallography

Single-crystal X-ray diffraction data were acquired on a Bruker D8 Venture diffractometer employing Mo-Kα radiation. Structure solution was achieved via intrinsic phasing methods using ShelXT program, followed by full-matrix least-squares refinement against F^2 using ShelXL implemented within the Olex^2 software package. The crystallographic coordinates for these structures have been deposited at the Cambridge Structural Database (CSD) under deposition number 2442298. The corresponding data can be accessed free of charge at http://www.ccdc.cam.ac.uk/data_request/cif.

UV−Vis−NIR Absorption and Reflection Spectra Measurements.

Powder samples underwent UV-Vis-NIR absorption and reflection measurements across 200–800 nm via an Agilent Cary 5000 spectrophotometer.

Fig. S1 presents the experimental powder X-ray diffraction (PXRD) pattern of $Rb_2Au_2I_6$ alongside the pattern simulated from its single-crystal structure. The correspondence of all observed diffraction peaks with the simulated pattern confirms the phase purity of the $Rb_2Au_2I_6$ powder sample. Characterization studies detailed herein were performed on these synthesized pure-phase single crystals or powders.

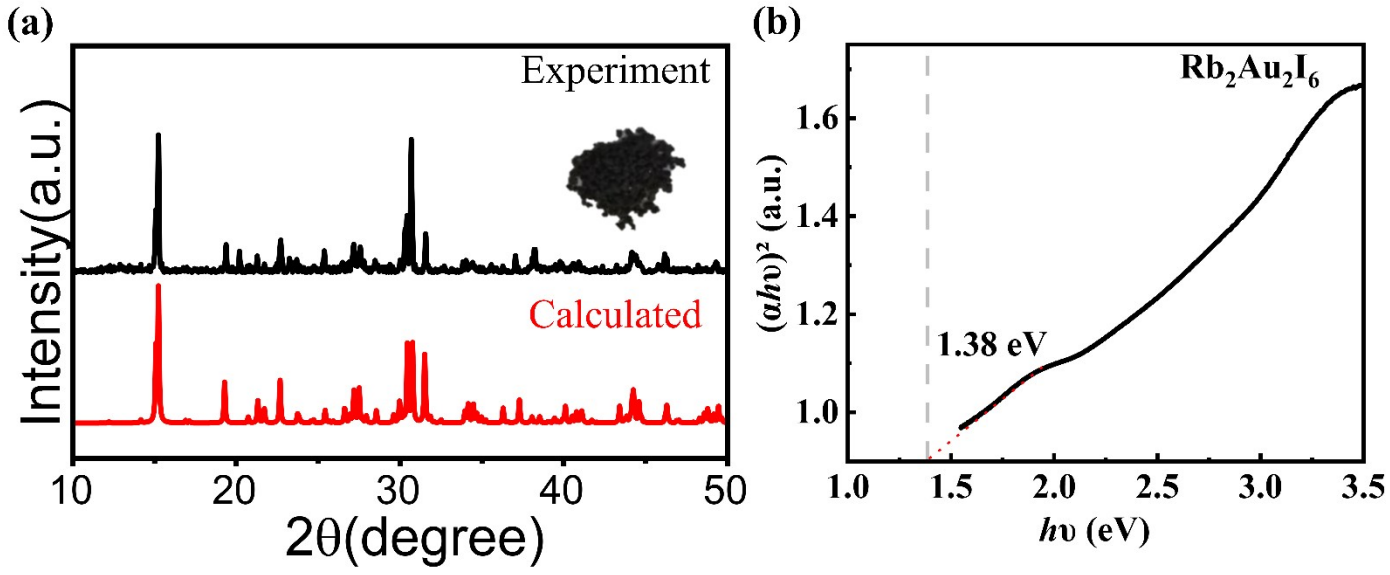

Figure S1. (a) PXRD pattern of *mP*-$Rb_2Au_2I_6$ with the calculated XRD pattern of the single crystal. (b) Optical band gap of *mP*-$Rb_2Au_2I_6$ determined from UV-Vis absorption spectra using the Tauc-plot method.

Table S1. Shannon radii of elements at sites A, B^+, B^{3+} and X.

A^+(Å)	B^+(Å)	B^{3+}(Å)	X^-(Å)	
Rb^+	Au^+	Au^{3+}	Cl^-	I^-
1.72	1.37	0.85	1.81	2.20

Table S2. Structural Factors of $Rb_2Au_2I_6$ and $Rb_2Au_2Cl_xI_{6-x}$ (x = 2, 3, 4) were calculated. The lattice parameters and unit cell volumes were optimized based on the PBE functional. Experimental results are listed in parentheses for comparison.

	t	μ_f	***a*** **(Å)**	***b*** **(Å)**	***c*** **(Å)**	***V*** **(Å^3)**
mC-$Rb_2Au_2I_6$	0.83	0.50	13.45 (13.45)	7.87 (7.87)	7.64 (8.77)	808.71 (928.32)
mP-$Rb_2Au_2I_6$	0.83	0.50	7.69 (7.48)	9.81 (9.19)	11.81 (11.72)	890.93 (805.65)
mC-$Rb_2Au_2Cl_2I_4$	0.84	0.54	11.84	7.30	8.71	752.82
mC-$Rb_2Au_2Cl_3I_3$	0.85	0.55	12.53	7.45	8.48	791.60
mC-$Rb_2Au_2Cl_4I_2$	0.85	0.57	12.75	7.79	8.33	827.36
mP-$Rb_2Au_2Cl_2I_4$	0.84	0.54	7.48	9.38	11.71	821.60
mP-$Rb_2Au_2Cl_3I_3$	0.85	0.55	7.45	9.39	11.29	789.80
mP-$Rb_2Au_2Cl_4I_2$	0.85	0.57	7.49	8.90	11.14	742.60

Table S3. The effective masses (in units of the free electron mass, m_0) along various directions were computed for *mC*-$Rb_2Au_2Cl_4I_2$, *mP*-$Rb_2Au_2Cl_2I_4$ using the HSE06+SOC functional.

	m^*_e/m_0	m^*_h/m_0
mC-$Rb_2Au_2Cl_4I_2$	1.64 ($Y \longrightarrow$ C)	3.94 ($\Gamma \longrightarrow Y$)
mC-$Rb_2Au_2Cl_4I_2$	2.65 (Y $\longrightarrow \Gamma$)	5.82 ($\Gamma \longrightarrow Z$)
mP-$Rb_2Au_2Cl_2I_4$	0.58 ($Z \longrightarrow \Gamma$)	3.22 ($Z \longrightarrow \Gamma$)
mP-$Rb_2Au_2Cl_2I_4$	0.45 ($Z \longrightarrow A$)	2.40 ($Z \longrightarrow A$)

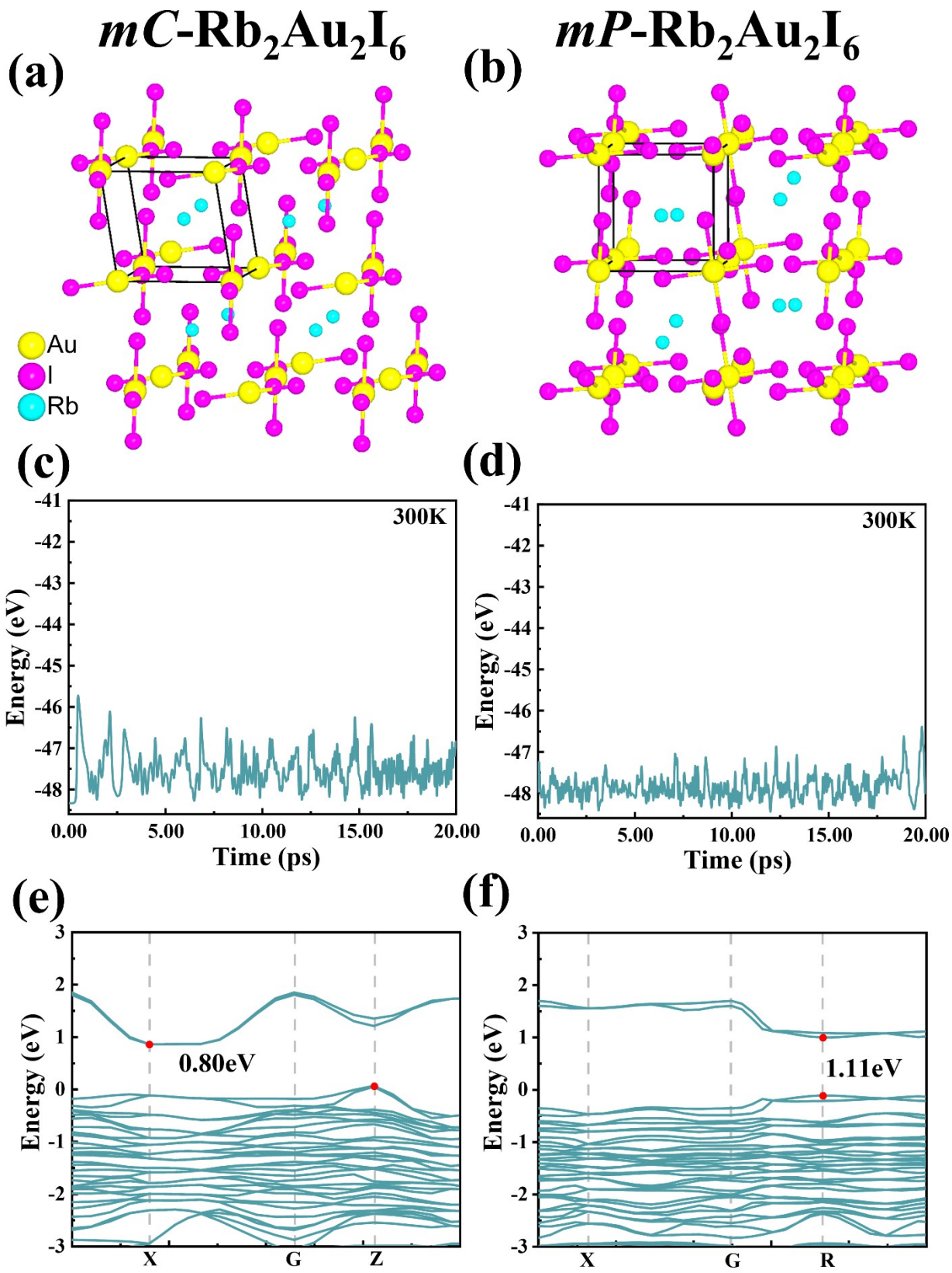

Figure S2. Octahedral framework representations of $Rb_2Au_2I_6$ with space group (a) *mC* and (b) *mP*. Total energies from ab initio molecular dynamics (AIMD) simulations for $Rb_2Au_2I_6$ in space groups (c) *mC* and (d) *mP*. The simulations were performed in the canonical (NVT) ensemble at 300 K using a 1×1×1 primitive cell, a time step of 1 fs, and a total trajectory length of 20 ps. Band structures of $Rb_2Au_2I_6$ in space groups (e) *mC* and (f) *mP*, calculated using the HSE06 functional with spin-orbit coupling (SOC).

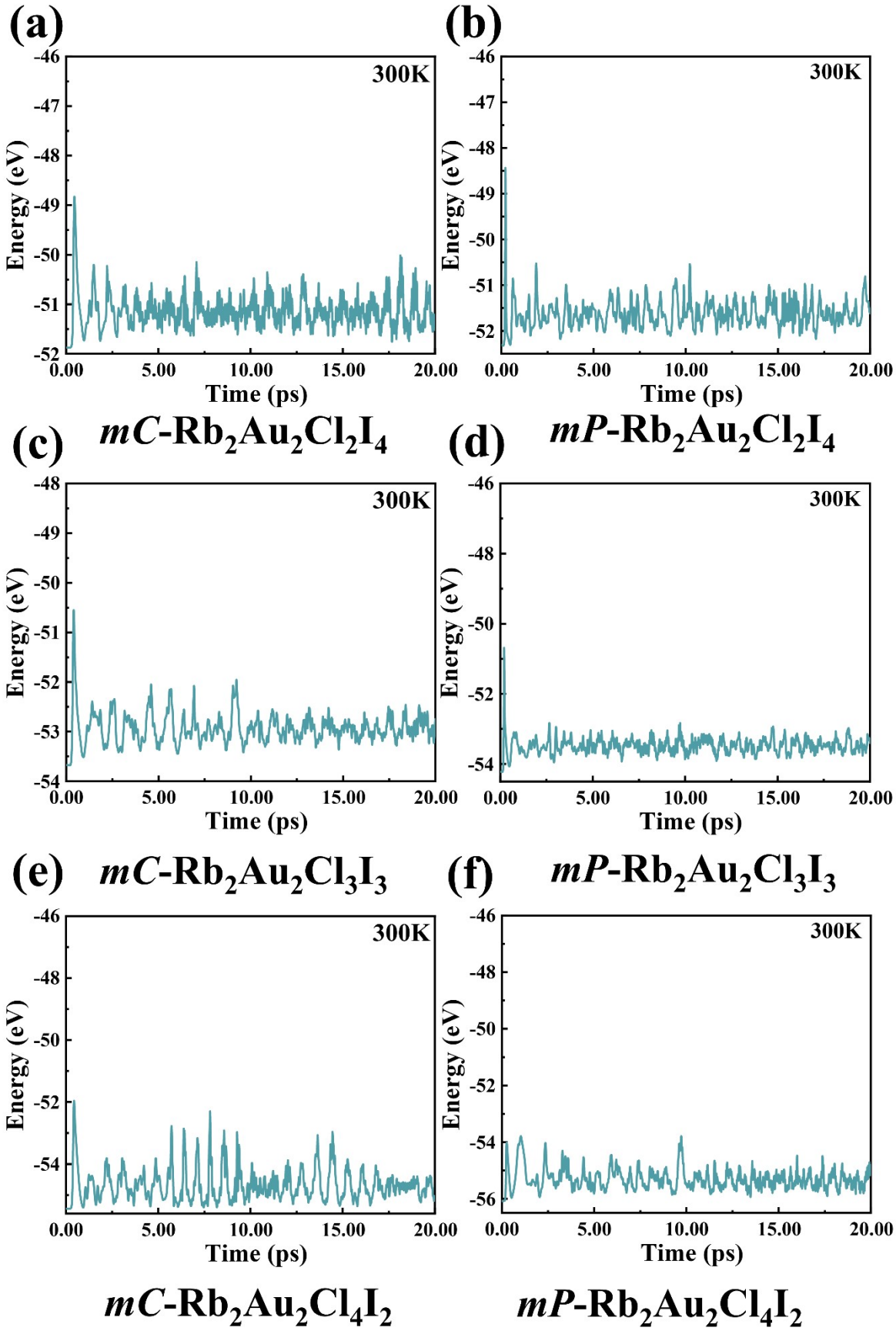

Figure S3. Total energies from AIMD simulations for $Rb_2Au_2Cl_xI_{6-x}$ (x=2, 3, 4) with different phases. The simulations were performed in the canonical (NVT) ensemble at 300 K using a 1×1×1 primitive cell, a time step of 1 fs, and a total trajectory length of 20 ps.

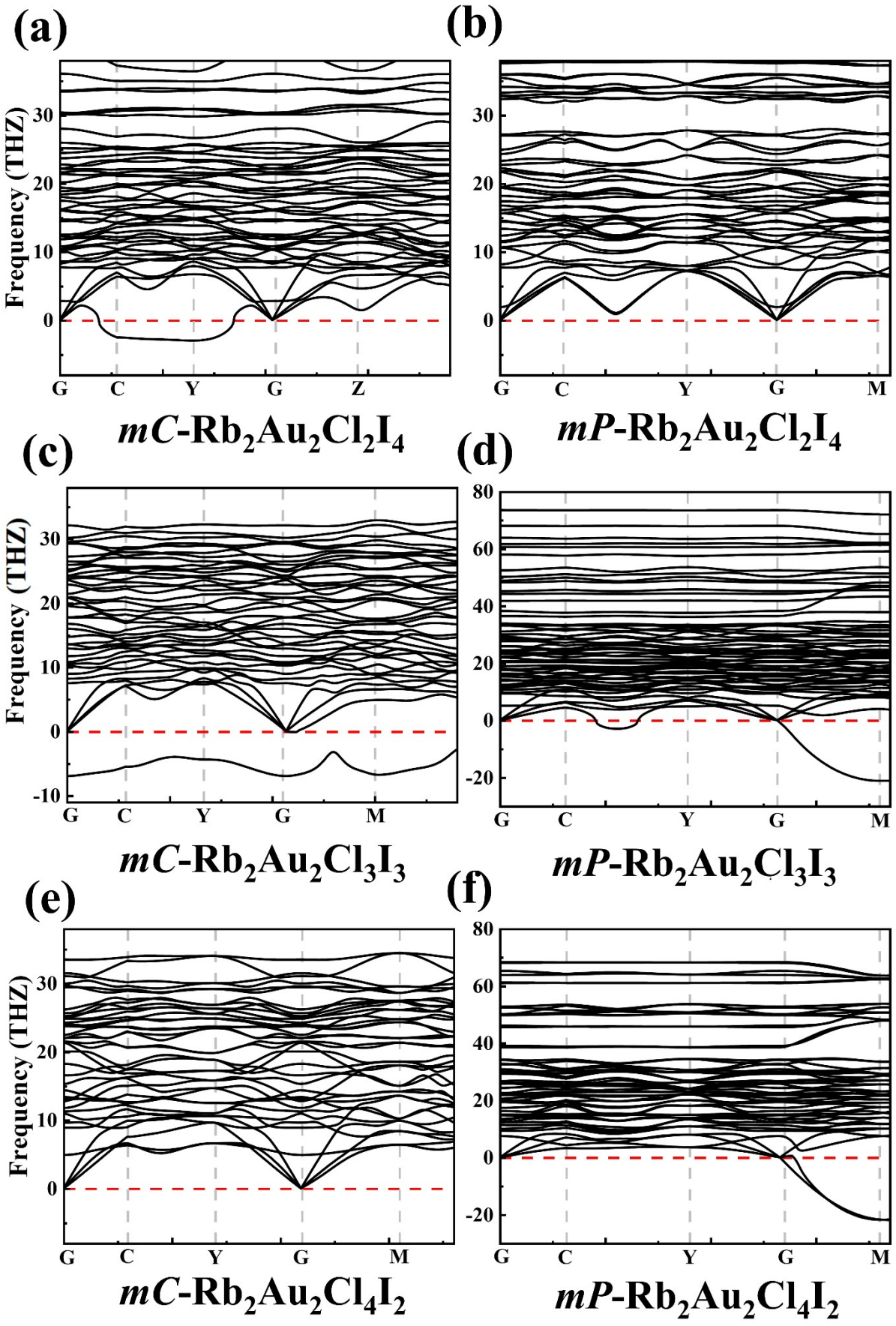

Figure S4. Phonon dispersion spectra for $Rb_2Au_2Cl_xI_{6-x}$ (x=2, 3, 4) with different phases.

Table S4. The optoelectrical parameters used in MCD simulations. The parameters for *mC*-$Rb_2Au_2Cl_4I_2$ and *mP*-$Rb_2Au_2Cl_2I_4$ were calculated quantum mechanically.

Parameter	***mC*-$Rb_2Au_2Cl_4I_2$**	***mP*-$Rb_2Au_2Cl_2I_4$**	**FTO**
Temperature (*T*)	300K	300K	300K
Band gap (E_{gap} in eV)	1.24	0.97	3.50
Relative dielectric constant (ε_r)	8.08	13.40	10.00
Electron mobility (μ_e in $cm^2 \cdot V^{-1} \cdot S^{-1}$)	1.33	55.70	100.00
Hole mobility (μ_h in $cm^2 \cdot V^{-1} \cdot S^{-1}$)	0.17	0.26	20.00